

Radar Reflectivity–Based Model Initialization Using Specified Latent Heating (Radar-LHI) within a Diabatic Digital Filter or Pre-Forecast Integration

STEPHEN S. WEYGANDT,^a STANLEY G. BENJAMIN,^a MING HU,^a CURTIS R. ALEXANDER,^a
TATIANA G. SMIRNOVA,^{b,a} AND ERIC P. JAMES^{b,a}

^aNOAA/Global Systems Laboratory, Boulder, Colorado

^bCooperative Institute for Research in Environmental Sciences, University of Colorado Boulder, Boulder, Colorado

(Manuscript received 30 August 2021, in final form 3 May 2022)

ABSTRACT: A technique for model initialization using three-dimensional radar reflectivity data has been developed and applied within the NOAA 13-km Rapid Refresh (RAP) and 3-km High-Resolution Rapid Refresh (HRRR) regional forecast systems. This technique enabled the first assimilation of radar reflectivity data for operational NOAA forecast models, critical especially for more accurate short-range prediction of convective storms. For the RAP, the technique uses a diabatic digital filter initialization (DFI) procedure originally deployed to control initial inertial gravity wave noise. Within the forward-model integration portion of diabatic DFI, temperature tendencies obtained from the model cloud/precipitation processes are replaced by specified latent heating–based temperature tendencies derived from the three-dimensional radar reflectivity data, where available. To further refine initial conditions for the convection-allowing HRRR model, a similar procedure is used in the HRRR, but without DFI. Both of these procedures, together called the “Radar-LHI” (latent heating initialization) technique, have been essential for initialization of ongoing precipitation systems, within all NOAA operational versions of the 13-km RAP and 3-km HRRR models extending through the latest implementation upgrade at NCEP in 2020. Application of the latent heat–derived temperature tendency induces a vertical circulation with low-level convergence and upper-level divergence in precipitation systems. Retrospective tests of the Radar-LHI technique show significant improvement in short-range (0–6 h) precipitation system forecasts, as revealed by reflectivity verification scores. Results presented document the impact on HRRR reflectivity forecasts of the radar reflectivity initialization technique applied to the RAP alone, HRRR alone, and both the RAP and HRRR.

SIGNIFICANCE STATEMENT: The large forecast uncertainty of convective situations, even at short lead times, coupled with the hazardous weather they produce, makes convective storm prediction one of the most significant short-range forecast challenges confronting the operational numerical weather prediction community. Prediction of heavy precipitation events also requires accurate initialization of precipitation systems. An innovative assimilation technique using radar reflectivity data to initialize NOAA operational weather prediction models is described. This technique, which uses latent heating specified from radar reflectivity (and can accommodate lightning data and other convection/precipitation indicators), was first implemented in 2009 at NOAA/NCEP and continues to be used in 2022 in the NCEP-operational RAP and HRRR models, making it a backbone of the NOAA rapidly updated numerical weather prediction capability.


KEYWORDS: Thunderstorms; Radars/Radar observations; Data assimilation; Numerical weather prediction/forecasting; Regional models

1. Introduction

Accurate prediction of the initiation and evolution of precipitation systems, especially of convective storms, has remained a major forecast challenge. Skillful prediction of mesoscale environmental fields is a prerequisite, including temperature, moisture, and winds in the lower troposphere and, especially, in the boundary layer. For the warm-season convective initiation (CI) challenge, in which potentially large areas of positive convective available potential energy (CAPE) exist, accurate analysis and prediction of small

capping inversions and weak forcing mechanisms are crucial. Frequent data from surface stations, satellites, and aircraft all play a key role over the United States in providing the synoptic observations needed to improve short-range forecasts of mesoscale convective environments. At night, the CI forecast problem is more difficult, as CI is often rooted above the surface layer, decreasing the utility of surface observations.

For ongoing precipitation systems, the U.S. national network of WSR-88D radars (Kelleher et al. 2007; Zhang et al. 2011, 2016) provides an invaluable set of observations. These observations have greatly improved operational thunderstorm warning and nowcasting and spurred research on computationally efficient methods for using these observations to initialize operational models. Over the past 25 years, a variety of effective, but computationally intensive methods, for variational and ensemble-based assimilation of radar data have been

 Denotes content that is immediately available upon publication as open access.

Corresponding author: Stephen S. Weygandt, stephen.weygandt@noaa.gov

DOI: 10.1175/WAF-D-21-0142.1

© 2022 American Meteorological Society. For information regarding reuse of this content and general copyright information, consult the [AMS Copyright Policy \(www.ametsoc.org/PUBSReuseLicenses\)](https://www.ametsoc.org/PUBSReuseLicenses).

demonstrated (e.g., Sun and Crook 1997, 1998; Caya et al. 2005; Aksoy et al. 2009, 2010; Wang et al. 2013; Wheatley et al. 2015; Gustafsson et al. 2018; Wang et al. 2019). Wattrelot et al. (2014) describe their approach in AROME-France to assimilate retrieved relative humidity (RH) profiles derived from radar reflectivity observations; they considered derived estimates of RH superior to direct reflectivity observations for data assimilation (DA) due to higher predictability of RH as compared to hydrometeor size distributions. Approaches for assimilation of radar data vary from “proxy” assimilation techniques like latent heat nudging (e.g., Jones and Macpherson 1997), to indirect variational assimilation of hydrometeors derived from observed reflectivity (e.g., Chen et al. 2021), to direct variational assimilation (e.g., Hawkness-Smith and Simonin 2021).

The large forecast uncertainty associated with convective situations, even at very short lead times, coupled with the severity of weather often associated with convective storms, makes convective storm prediction one of the most significant short-range forecast challenges confronting the operational numerical weather prediction community. As an example, the commercial aviation industry is particularly vulnerable to convective storms, with resulting flight delays and diversions spiking every summer (e.g., Sauer et al. 2019). Prediction of severe thunderstorms, tornadoes, and convective heavy rainfall events also requires accurate initialization of convective storms. Even in larger-scale winter storms, bands and small-scale areas of heavy snow and mixed precipitation are driven by rapidly changing local circulations related in part to latent heat release within these systems.

To that end, a radar–data assimilation technique was developed that requires negligible additional computational resources, while allowing effective use of radar reflectivity data for improved hourly updated weather predictions from the NOAA 13-km Rapid Refresh (Benjamin et al. 2016; B16) and 3-km High-Resolution Rapid Refresh (HRRR; B16, Dowell et al. 2022, hereafter D22; James et al. 2022, hereafter J22) models. The North American domain for RAP and the lower-48 U.S. domain for HRRR are shown in Fig. 2 in D22. The technique described in this paper uses radar observations to estimate latent heating for model initialization of precipitation systems (denoted herein as radar latent heating initialization or “Radar-LHI”), thereby achieving an effective radar reflectivity data assimilation method, the first such used in a NOAA operational weather model.

Latent heating (LH) from the conversion of water vapor to liquid/ice phase is an essential driver for upward vertical motion on both the convective scale and the synoptic scale. Danard (1964) summarized the effects of LH on cyclone development using the ω equation. Fiorino and Warner (1981) showed how specification of latent heating could help with hurricane initialization. Wang and Warner (1988) provided an example of LH specification during a sequence of 1-h periods for a severe weather case using a model with 30-km grid spacing. Since then, applications of specifying LH for radar/precipitation DA has been demonstrated by Jones and Macpherson (1997) and, more recently, by the Canadian mesoscale model (Jacques et al. 2018). Other studies describing

LH specification or “nudging” include Leuenberger and Rossa (2007), Stephan et al. (2008), Huang et al. (2018), and Huo et al. (2021). However, none of these have used LH specification within DFI as described in this paper. An alternate radar-assimilation strategy to LH specification has been to directly specify relative humidity profiles (e.g., Wattrelot et al. 2014; Martet et al. 2022) instead of letting LH-induced vertical motion result in higher relative humidity. A summary of different radar-reflectivity DA techniques including direct use of radar reflectivity as a state variable is provided in Duda et al. (2019). Observations or estimates of condensate from remote sensing via radar, ground- or satellite-based lightning sensors, or satellite precipitation estimates can be a powerful addition for data assimilation via the radar-LHI technique or other radar-DA methods.

We describe in this paper the radar-LHI technique that has been developed and applied to both the 13-km RAP and the 3-km HRRR models. This general radar-LHI technique includes two related specific procedures using estimated latent heating primarily from a national mosaic of radar reflectivity data: one procedure for initializing the RAP model and a second procedure for further refining initial conditions for the HRRR model. For the RAP, the procedure uses a diabatic digital filter initialization (DFI, Huang and Lynch 1993; Lynch and Huang 1994) to apply the latent heating (denoted as “radar-LH-DFI” in this paper). For the HRRR, the procedure uses a forward model integration (during a pre-forecast hour) to apply the latent heating (denoted as “forward-radar-LH” in this paper).

The operational RAP and HRRR (through 2022 with the RAPv5/HRRRv4) use both of these related procedures and include a simple method for incorporation of lightning data from land-based networks via a lightning-based proxy reflectivity, as described by Weygandt et al. (2008) and B16. For versions through RAPv4/HRRRv3, the radar-LH-DFI-initialized RAP fields provided a background for the HRRR forward-radar-LH. This RAP-HRRR linkage was modified in the HRRRv4, with the introduction of the HRRR Data Assimilation System (HRRRDAS) 3-km ensemble data assimilation described by D22. More information on the use of the various assimilation algorithms in the different operational versions of the HRRR is given in section 3 of D22 (especially their Fig. 3 and sections 3c and 3d). In addition, a severe convection case study comparison of HRRRv3 versus HRRRv4 is shown in D22 (their section 4b and Fig. 5). The HRRRv3 includes use of the radar-LH-DFI assimilation procedure in the parent RAP model and the forward-radar-LH procedure in the HRRR. For the HRRRv4, the HRRRDAS-based ensemble assimilation algorithm is used (for radar reflectivity as well as conventional observations) in addition to the HRRR-based forward-radar-LH. Also, the HRRRv4 does not directly benefit from the RAP radar-LH-DFI because the RAP fields have been replaced by the HRRRDAS ensemble mean fields for initializing the HRRR pre-forecast hour (but the RAP fields are used as input to the HRRRDAS as described in section 3d of D22). In this paper, we describe both the RAP and the HRRR radar-LHI procedures, provide illustrative examples of their effectiveness, and show

TABLE 1. Significant events related to radar reflectivity processing and assimilation using Radar-LHI for the hourly updated NOAA Rapid Update Cycle (RUC), Rapid Refresh (RAP), and High-Resolution Rapid Refresh (HRRR) models.

| Year | Event |
|------|---|
| 1998 | Application of adiabatic digital filter initialization (DFI) in RUC model |
| 2006 | Application of diabatic DFI in RUC model |
| 2006 | CONUS 3D radar reflectivity mosaic developed by NSSL (Multi-Radar Multi-Sensor) |
| 2008 | Initial radar-LHI through diabatic DFI (radar-LH-DFI) in 13-km operational RUC |
| 2012 | Radar-LHI through diabatic DFI (radar-LH-DFI) in 13-km RAP version 1 |
| 2014 | Radar-LHI (forward-radar-LH) added through 1-h pre-forecast in 3-km HRRRv1 |
| 2016 | Updated radar-LHI in RAPv3/HRRRv2 |
| 2018 | Further update to radar-LHI for RAPv4/HRRRv3 |
| 2020 | Introduction of 3km-ensemble DA for HRRRv4 (D22), retain radar-LHI |

statistical skill assessments of the use of the two procedures individually and in combination.

2. Description of the radar reflectivity latent heating initialization technique

The Radar-LHI technique described in this section complements the 3-km ensemble data assimilation described in D22. An overview of the DA flowcharts for HRRRv1–3 (with Radar-LHI) versus HRRRv4 is provided in Fig. 3 in D22. Details about the configuration of the HRRR forecast model are provided in D22. For both the RAP and HRRR applications, the radar-LHI technique relies on specification of a three-dimensional (3D) latent heating field from the 3D gridded national radar reflectivity mosaic data provided by the Multi-Radar Multi-Sensor (MRMS, Zhang et al. 2011, 2016) product. The real-time MRMS feed of 3D gridded national mosaic reflectivity data, covering the contiguous United States, has been essential for the development and operational implementation of the radar-LHI model initialization technique.

The mapping of 3D radar reflectivity to 3D latent heating on the model grid uses the following relationship:

$$\text{LH}(i, j, k) = \left\{ \left[\frac{1000}{p(i, j, k)} \right]^{R_d/C_p} \times \left\{ (L_v + L_f) f[\text{Ze}(i, j, k)] / (C_p \Delta t_{\text{cond}}) \right\} \right\}, \quad (1)$$

where LH is the latent heating rate (in K s^{-1} ; potential temperature change rate), p is pressure (hPa) on the 3D (i, j, k) model grid points, and thermodynamic constants (C_p , R_d , L_v , L_f) have their normal definitions. The $f(\text{Ze})$ term represents the conversion of the local radar reflectivity to rain condensate mixing ratio based on Marshall and Palmer (1948). The simplifying assumption to convert the reflectivity to just rainwater

reflects the under-determinism in the mapping of reflectivity to hydrometeors. The inclusion of L_f may lead to slightly exaggerated heating in some cases, but may provide a better estimate of the total latent heating for deep convection in mid latitudes. The term Δt_{cond} is an assumed time period over which this full condensate is produced from water vapor—in essence, a convective cloud time scale. Details on assumed Δt_{cond} values for both the RAP and HRRR are provided below (including in Table 2).

This specification of latent heating from reflectivity is subject to the following conditions. Latent heating is only calculated where the MRMS reflectivity exceeds 28 dBZ, thereby restricting application of the heating to regions with active ongoing convection or moderate or greater active condensation processes. The latent heating rate is set to zero where the observed reflectivity is less than or equal to 0 dBZ, leading to a “suppression” of spurious convection/precipitation processes that may exist in the model fields. For regions that are outside the 3D radar mosaic coverage or regions where the reflectivity values are between 0 and 28 dBZ, the model-computed temperature tendency is retained. This 28-dBZ lower threshold restricts the heating to regions of moderate to strong condensate production, for which latent heating is likely a significant factor driving the local atmospheric evolution.

For radar observed volumes with at least 200 hPa of depth (after interpolation to the model grid), radar-based temperature tendencies are extended from the lowest observed level down to the model-defined top of the well-mixed planetary boundary layer for each grid column. This extension addresses adverse impacts that can occur from vertically limited areas of high level heating due to limitations in low-level radar coverage. Additional RAP and HRRR model application details are described in the following subsections.

TABLE 2. Condensation time period (Δt_{cond}) applied to calculate latent heating from radar reflectivity for versions of RUC, RAP, and HRRR (year of NCEP model implementation indicated in parentheses). Condensate inferred from reflectivity is assumed to be formed over this time period, roughly a convective-cloud time scale.

| | RUC (2008) | RAPv1 (2012) | RAPv2/HRRRv1 (2014) | RAPv3/HRRRv2 (2016) | RAPv4/HRRRv3 (2018) | RAPv5/HRRRv4 (2020) |
|----------------------------------|---------------|-----------------|------------------------|------------------------|------------------------|------------------------|
| Condensation Δt —DFI | 30 min | 10 min | 10 min | 10 min | 20 min | 20 min |
| Condensation Δt —forward | — | — | 20 min | 20 min | 20 min | 20 min |

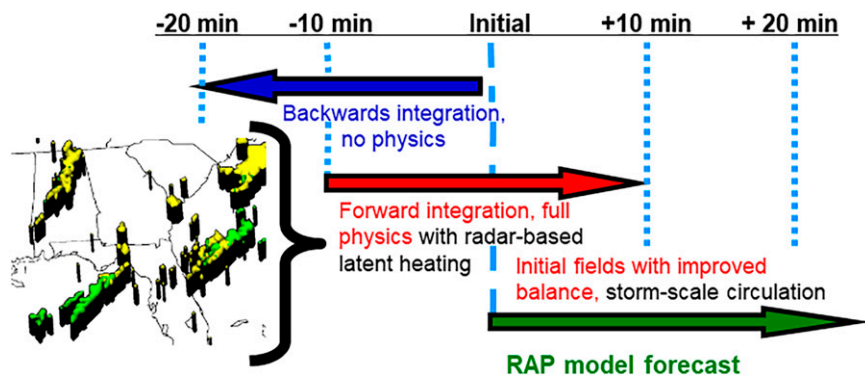


FIG. 1. Application of specified latent heating within the diabatic DFI used in the Rapid Refresh model (denoted as “radar-LH-DFI”). Three-dimensional latent heating is specified for the forward DFI from radar reflectivity data (in yellow and proxy lightning data are in green) as described in the text.

a. Diabatic DFI with radar reflectivity initialization (radar-LH-DFI) in RAP

As part of the model initialization procedure for the RAP model, a backward–forward diabatic DFI (Huang and Lynch 1993; Lynch and Huang 1994) is applied to control inertial gravity waves that may be generated by imbalances resulting from the model analysis, as described by Peckham et al. (2016) and B16 (their sections 2c and 2d). This application of a DFI dates back to the NOAA hourly updated Rapid Update Cycle (RUC) model (see Fig. 2 of Benjamin et al. 2004) run at NCEP through 2012 (Table 1) and has been essential for the hourly assimilation cycle. The original DFI application in the RUC used an adiabatic filter (Lynch and Huang 1992), but was upgraded to allow for a diabatic forward integration in 2006 to improve initial water vapor fields. This diabatic DFI application incorporated subgrid-scale model processes including boundary layer and cloud/diabatic processes within its resulting balance, and also allowed for a radar reflectivity initialization procedure using the model.

Application of the diabatic DFI, including the radar-LH-DFI procedure within the RAP model integration, is shown in Fig. 1. The model first runs backward without diabatic or viscid processes (Peckham et al. 2016) for a short period (20 min in this case), applying the digital filter weighting to values from each time step during this backward integration. A weighted average of these model states provides a new model state valid at the midpoint of the backward integration ($t = -10$ min in this case). Starting with this new state, a full-physics (with diabatic and viscid processes) version of the model is then integrated forward in time for the same time length, while accumulating a digital-filter-weighted mean from the model states at each time step, yielding a new model state valid at the original model initial time ($t = 0$ min). As noted above, this RAP-only procedure within radar-LHI is designated as radar-LH-DFI.

To illustrate the application of DFI to improve balance in initial conditions, Fig. 2 shows the time evolution of a model noise parameter $|dp_s/dt|$ (Huang and Lynch 1993; Benjamin et al. 2004) with and without DFI for the RAP model. This

noise parameter (domain-mean absolute surface pressure change calculated each time step, capturing high-frequency oscillations) is shown for the backward and forward model integrations during the DFI and then for the subsequent free-forecast. Comparison of the two free-forecast curves illustrates the significant noise reduction provided by the DFI during the first few hours of the model free-forecast. The diabatic DFI has been used effectively in both the RUC and the RAP, with application each hour resulting in quieter 1-h forecasts, leading to smaller observation-forecast analysis innovations, and in turn to further quieter subsequent 1-h forecasts.

For the addition of the radar-LH-DFI procedure in the diabatic DFI (Fig. 1), a simple change is made within the full physics forward model portion of the DFI, namely, the prognostic temperature tendencies computed at each time step from the explicit microphysics scheme and the cumulus parameterization scheme are replaced by a three-dimensional temperature latent heating–based tendency derived from the 3D radar reflectivity data. A latent heating contribution from land-based lightning data networks is also included (Weygandt et al.

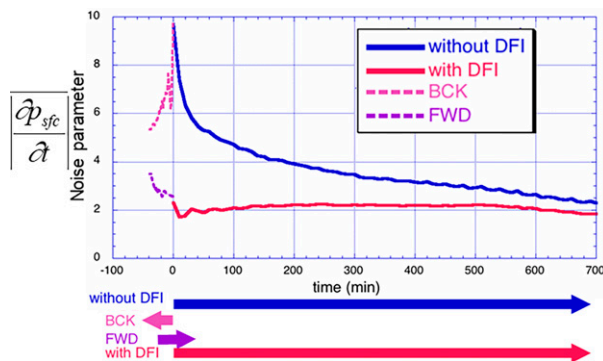


FIG. 2. Noise parameter [mean absolute surface pressure tendency (hPa hr^{-1}) averaged over domain] for Rapid Refresh using diabatic DFI application, including specification of latent heating from radar and lightning data. DFI was applied over a 40-min period in this test, but the normal DFI period for RAP is 20 min, as shown in Fig. 1.

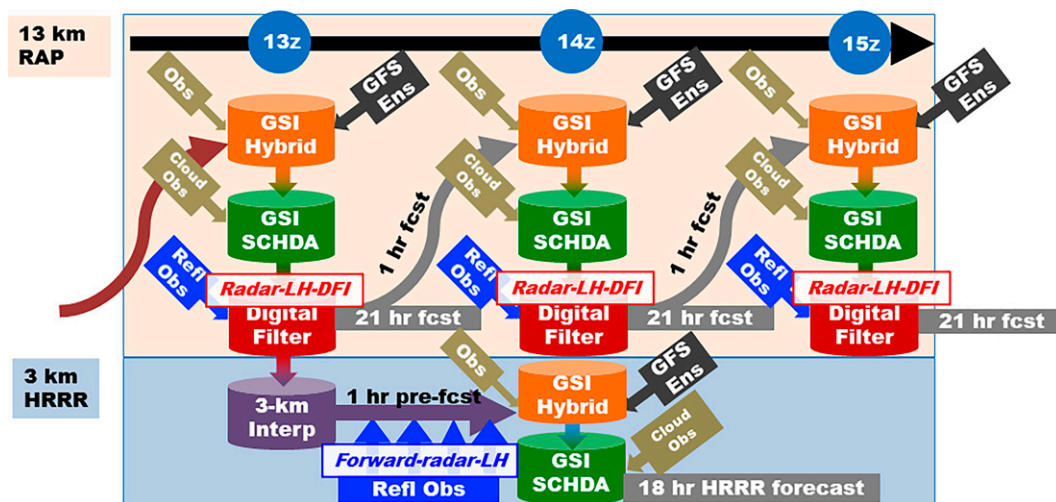


FIG. 3. Data assimilation flow diagram for the hourly updated Rapid Refresh (v4) and HRRR (v3) models. (Updated from Fig. 2 in B16 for a more recent version of the Rapid Refresh.) Application of radar (and proxy lightning) reflectivity through latent heating (radar-LHI) is indicated by the dark blue boxes/arrows and italics text in boxes, including application of the temperature tendency within the diabatic DFI (red italics “Radar-LH-DFI”) for the 13-km RAP and within the 1-h pre-forecast integration for the 3-km HRRR (blue italics “Forward-radar-LH”).

2008). Over the eastern portion of the WSR-88D coverage region, augmentation of the radar reflectivity-based latent heating field and resultant impacts from the lightning data are minimal, while slightly greater impacts from the lightning data are likely over the western portion of the WSR-88D region, due to limitations in the WSR-88D coverage (Kluzura and Imy 1993). For this application with the RAP, a condensation time period (Δt_{cond}) of 10 min was assumed. Values ranging from 5 to 20 min have been tested, and Table 2 provides a summary of the convective time scale used for both RAP and HRRR models for the various operational implementations. As can be seen in Table 2, a change to a longer time period (resulting in a reduction of the strength of the heating) occurred in the RAP with the RAPv4 operational implementation. The RAPv2/HRRRv1 values (which are the same as the RAPv3/HRRRv2 values) for Δt_{cond} from Table 2 are used for this study. For the RAP application, additional convective suppression is accomplished in regions with no reflectivity by restricting the activation of the convective parameterization (Grell and Freitas 2014), during the first 30 min of the otherwise free-forecast in these regions.

b. Overall RAP/HRRR radar reflectivity assimilation technique including forward integration with radar reflectivity initialization (forward-radar-LH) in HRRR

For the HRRR, the radar-LHI technique is applied in a different manner, as part of the overall RAP and HRRR model initialization procedures. Figure 3 provides a schematic workflow diagram illustrating steps taken for the RAP and HRRR model initialization, including the radar-LHI applications. The hourly RAP model initialization steps (indicated in the tan-shaded upper portion of Fig. 3) include applications of the following: 1) a GSI hybrid ensemble-3DVAR analysis using ensemble background covariance information provided from GDAS ensemble members (Hu et al. 2017) using a wide variety

of observations (see B16, their Table 4; D22, their section 3); 2) a stratiform cloud-hydrometeor data assimilation (SCHDA; Benjamin et al. 2021); and 3) the diabatic DFI with the radar-LH-DFI procedure (as described in the previous section), followed by the RAP free-forecast. For the HRRR, radar-based latent heating is applied in a forward-only 1-h spinup cycle (forward-radar-LH) as detailed below.

For the 3-km HRRR model, additional application of DFI was found to add no value over the forward-radar-LH and incurred more computational expense. In contrast, the forward-radar-LH procedure, in which MRMS-derived latent heating rate estimates are substituted in place of model-predicted values from the cloud microphysics temperature tendencies during a 1-h model pre-forecast period, was found to yield further benefit in addition to the RAP application of radar-LH-DFI. As indicated in Fig. 3, this forward-radar-LH procedure is included in the overall HRRR initialization steps, which include: 1) interpolation of the RAP post-radar-LH-DFI grids for all prognostic variables, including hydrometeors, from the previous hour to the HRRR 3-km grid, 2) completion of a 3-km 1-h pre-forecast numerical integration including application of the forward-radar-LH using radar observations, and 3) application of the GSI hybrid analysis and SCHDA at the model initial time (following the pre-forecast hour). It is important to note that all other components of the RAP/HRRR assimilation system depicted in the Fig. 3 flowchart (the RAP and HRRR applications of the GSI analysis and the SCHDA) are used, including assimilation of the standard sets of observations (see details in B16 and J22), and were not varied in the different experiments described in this study.

Details on the application of the HRRR forward-radar-LH procedure during the 1-h pre-forecast numerical integration are as follows. MRMS radar reflectivity fields from four times (45, 30, 15, and 0 min before the model free-forecast time) are used to derive latent heating-based temperature tendency

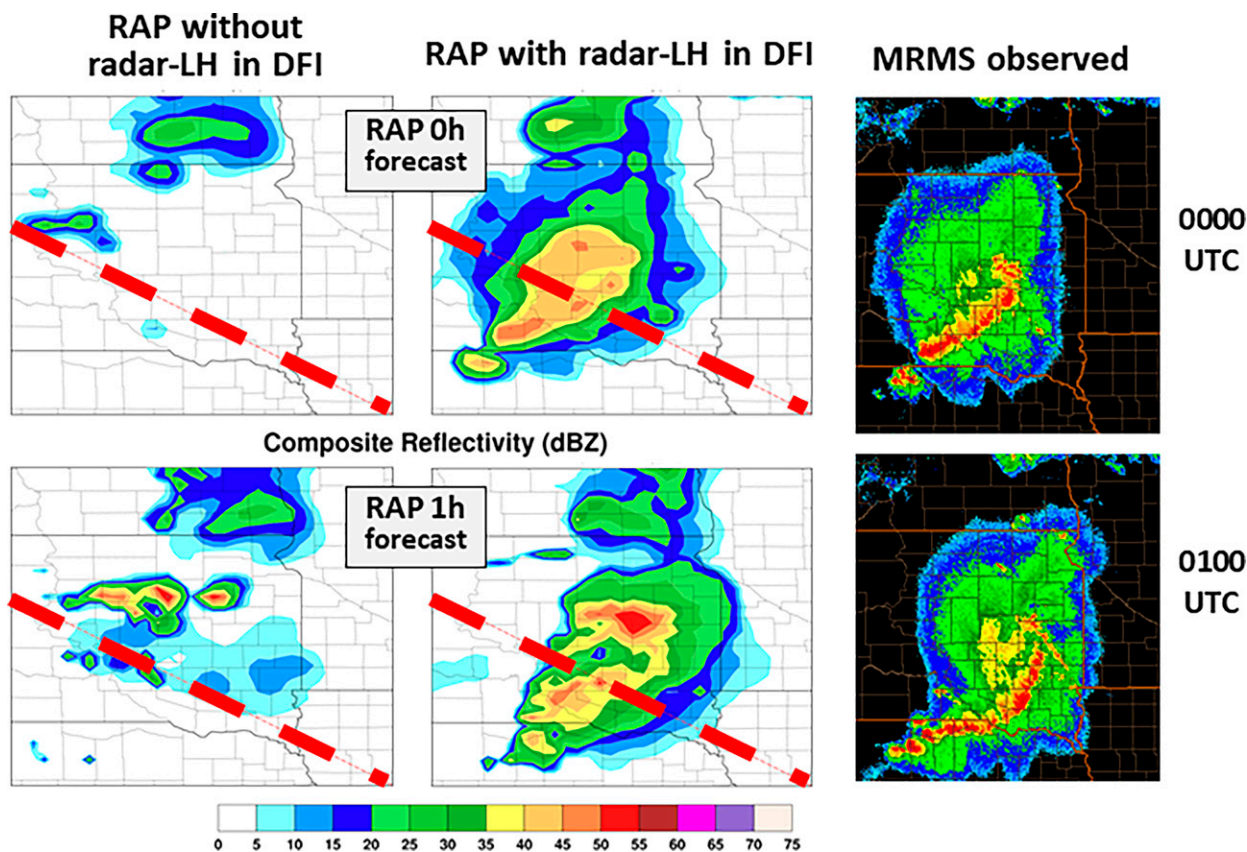


FIG. 4. Composite reflectivity for (top) 0000 and (bottom) 0100 UTC 12 Aug 2011 from RAP forecasts for initial conditions at 0000 UTC and from observations (composite reflectivity from MRMS). (left) Without radar-LH-DFI, (center) with radar-LH-DFI, and (right) observed. Red dashed line is location for cross sections in Fig. 5. Color bar for reflectivity (dBZ) is shown at the bottom of the figure.

fields that are prescribed (in place of the model microphysics scheme computed temperature tendency) for four successive 15-min periods during the pre-forecast integration period (60–45, 45–30, 30–15, and 15–0 min prior to the final model initialization time). This application of the heating during a period prior to the time of the observed radar reflectivity (from which the latent heating is computed) is considered to be a realistic configuration, as the processes generating the reflectivity would be occurring during a time prior to that observed reflectivity. The 15-min update of the observed radar reflectivity during the pre-forecast integration simply allows the latent heating to be based on the most recent evolving observed reflectivity.

c. Illustration of the impact of the radar-LHI on RAP model fields

To provide a sample illustration of the impact of the radar-LHI, we show selected RAP fields from a run with and without radar-LHI (specifically radar-LH-DFI for this RAP run). The case is from a 0000 UTC 12 August 2011 initialization of a squall line. Figure 4 shows a comparison of RAP model reflectivity fields (including an estimate from the convective parameterization of rain rate) with the observed composite (column-maximum) radar reflectivity mosaic for the 0-h model initial fields (after the DFI application) and the 1-h model free-forecast fields, for two runs: without the radar-

LHI (left column) and with the radar-LHI (center column). As can be seen, the radar-LHI technique results in a significant enhancement of the convective system, both in the 0-h model initial field (top row) and the 1-h model forecast field (bottom row), compared to the no radar-LHI run. It is important to note that analysis of the fields (not shown) indicates that, for this 13-km RAP case, the radar-LHI is projecting onto both parameterized convection (via the Grell–Freitas cumulus parameterization used in the RAP) and explicitly resolved hydrometeors (coarsely resolved explicit representation of the convective system). While the signal from the radar-LHI can clearly be seen, the largely parameterized 13-km model depiction of the convection is not able to adequately capture the observed squall-line details.

For the same case, Fig. 5 shows the corresponding vertical cross sections of RAP horizontal convergence (positive values indicate convergence, negative values indicate divergence) along a cross section through the convective system for the 0-h model initialization (top row) and the 1-h model forecast (bottom row). As can be seen in the column on the left (the run without the radar-LHI in the diabatic DFI) the convergence values are small, with no enhancement associated with the convective system. In contrast, the panel in the upper right (0-h model initialization after the DFI, with the radar-LHI) shows a clear pattern of low-level convergence (yellow to

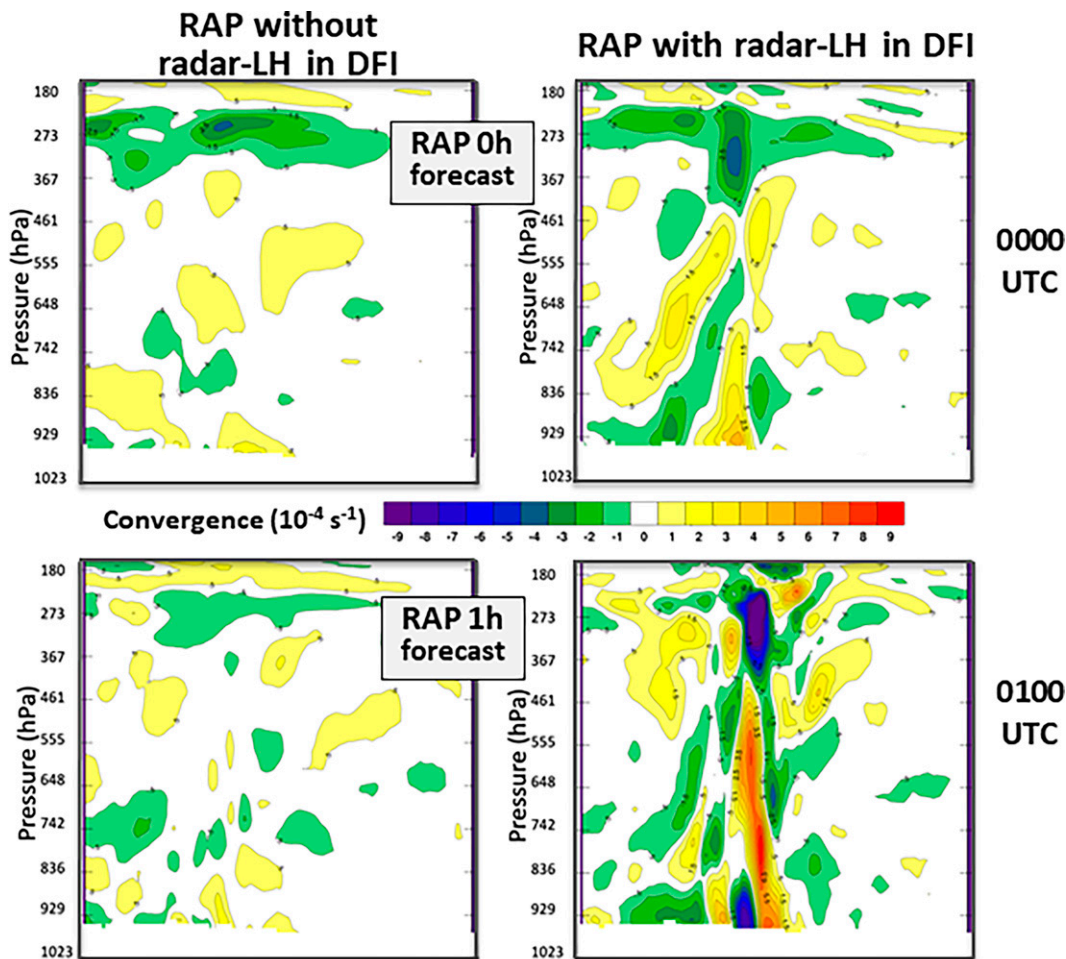


FIG. 5. Horizontal convergence in vertical cross sections along line from Fig. 4. (top) From RAP for initial conditions at 0000 UTC 12 Aug 2011 and (bottom) 1-h forecast at 0100 UTC 12 Aug 2011. Color bar for reflectivity (10^{-4} s^{-1}) is shown in the middle of the figure.

orange region near the ground) and accompanying upper-level divergence (green to blue shading) in the 200–300-hPa layer. As the lower right panel shows, this vertically aligned pattern intensifies during the first forecast hour, as the convection induced by the radar-LHI strengthens. Thus, heating associated with the temperature tendency specification in the radar-LHI induces these fields (and associated updraft), leading to a more pronounced convective evolution. Other tests (not shown) have indicated that, as expected, the response is modulated by the instability and other factors in the local environment within the model. The response is also modulated by the strength of the heating, which is controlled by the assumed convective time period (Δt_{cond}) in Eq. (1) and Table 2.

3. Radar-LHI retrospective study and results

We now present results from a retrospective study to illustrate the impact of the radar-LHI assimilation technique (applied within both the RAP and HRRR model) on HRRR model forecasts of reflectivity. The limited scope of this study does not include objective assessment of the impact of the

assimilation technique on other model fields, but in multiple years of operational application of this technique we have generally seen minimal systematic impacts on other fields (other than those specifically associated with the modifications to the precipitation regions). J22 provides extensive verification results from different versions of the operational RAP and HRRR. In section 3a, we describe the experiment design and in section 3b describe expected diurnal and regional aspects of the results. In section 3c, we show verification statistics (CSI and bias) to quantify the overall forecast performance from the four radar assimilation experiments and examine some diurnal and regional aspects of the verification. In section 3d, we complement the statistical assessment with examination of sample forecast reflectivity fields from the four experiments initialized at two different times of the day.

a. Experiment design

To document the impact of both the RAP-based and HRRR-based radar-LHI on HRRR forecast reflectivity fields, a retrospective experiment was conducted including 28 cases covering a broad range of initialization times across the diurnal

cycle during a 3-day period (17–19 May 2013). Table 3 provides a summary of the four different 15-h forecast experiments, designated with two letter identifiers, with the first letter (Y or N) indicating whether the radar-LH-DFI was performed in the RAP and the second letter (Y or N) indicating whether the forward-radar-LH was performed in the HRRR. We note that in all four experiments, the 13-km RAP is hourly cycled, and the digital filter initialization is included (but without the radar-LH-DFI for the NN and NY experiments) and the 3-km HRRR pre-forecast integration is included (but without the forward-radar-LH for the NN and YN experiments), followed by the application of the GSI and cloud analysis to the HRRR grids. The only aspect that is varied in the experiments is the specification of radar reflectivity-based latent heating (via the two different procedures of the “radar-LHI” technique in the two different models).

b. Expected diurnal and regional aspects

Based on the diurnal and regional characteristics of warm season convection (Carbone and Tuttle 2008; Fabry et al. 2017), as well as the regional WSR-88D radar coverage differences (Klazura and Imy 1993), we expect to see diurnal and regional differences in the impact from the radar data assimilation technique, which is confirmed in our experiences with the radar-LHI. In particular, we have seen a significant diurnal aspect to the performance, with greater impact from the radar-LHI for runs initialized during the evening and overnight hours and reduced impact for runs initialized during the daytime hours, especially right before the typical time for CI. This is to be expected, as in the absence of observed convection only the convection suppression aspect of the radar-LHI can yield forecast improvement. Thus, during the late morning through midday period of minimum convection during the warm season (across CONUS), we expect a minimum in forecast skill improvement from the radar-LHI. This somewhat extends into the period after CI as well, when the areal extent of convection is small and there is relatively less signal for the radar-LHI than during the later periods of the diurnal convective evolution. Conversely, during the evening and overnight hours, as the convection typically grows up-scale (and may not have been well represented with assimilation of just conventional observations), we expect a greater impact from the radar-LHI. Highlighting these diurnal aspects to the radar assimilation impact is a key part of our assessment.

We also expect to see regional differences, especially between the eastern and western United States. Warm-season convection in the eastern United States has a strong diurnal cycle, with a tendency for smaller-scale afternoon convection to grow up-scale and evolve into larger-scale convective systems continuing overnight and then dissipating in the morning hours the next day. Carbone and Tuttle (2008), Fabry et al. (2017), and other studies have well documented these regional and diurnal aspects to warm-season convection over the United States. In the western United States, warm-season convection is even more closely associated with the diurnal heating cycle, with significant dissipation of convection during the evening into overnight hours and fewer large-scale

TABLE 3. Retrospective experiments for the May 2013 test period. For each experiment performed, the component of radar-LHI in both the RAP and HRRR is indicated, as well as the condensation time period.

| Expt name | Radar-LH-DFI in RAP (Δt_{cond}) | Forward-radar-LH in HRRR (Δt_{cond}) |
|-----------|--|---|
| NN | No | No |
| YN | Yes (10 min) | No |
| NY | No | Yes (20 min) |
| YY | Yes (10 min) | Yes (20 min) |

convective systems (compared to the eastern United States). Western U.S. convection also is strongly tied to local terrain forcing and has a smaller scale than eastern U.S. convection. Areas of elevated convection (much of it nocturnal) are also more common in the eastern United States. There are also significant WSR-88D radar coverage differences between the eastern and western United States (Klazura and Imy 1993). This affects both the radar assimilation across the west (where augmentation with lightning data is likely more helpful than in the east) and radar verification in the West (due to the reduced radar observation coverage). While a detailed assessment of regional aspects of the radar assimilation impact is beyond the scope of this paper, we show selected statistical results from both the eastern and western United States, highlighting how regional differences affect the diurnal aspects of the radar data assimilation impact.

c. Reflectivity skill score assessment

To quantify the overall impact on model reflectivity forecasts for each of the four experiments, values for two categorical skill scores (applied to the forecast reflectivity field) are shown for the four experiments. The scores are the critical success index (CSI; Doswell et al. 1990) and the frequency bias computed for the 30-dBZ threshold over verification domains covering the eastern and western United States (divided by 100°W longitude), using the MRMS composite reflectivity mosaic as verification truth. To provide some degree of a “neighborhood” skill assessment (Weygandt et al. 2004; Ebert 2009), the CSI is computed after the forecasts and MRMS mosaic have been upscaled to a 20-km grid using a budget interpolation procedure designed to preserve area-averaged values. Based on extensive assessments of CSI scores for this and similar retrospective case studies, we have found that this combination of reflectivity threshold and upscaling values provides a good quantification of forecast skill that agrees well with our subjective assessments.

CSI and frequency bias scores, averaged over the entire 28-run retrospective study, are shown as a function of forecast length in Fig. 6, for both eastern (E) and western (W) U.S. verification regions. Examination of the CSI scores as functions of forecast length for both E and W indicates very similar overall performance for the three experiments that have radar-LHI applied on at least one of the grids (RAP or HRRR), with high CSI scores at the initial time decreasing fairly rapidly during the first two forecast hours, then more gradually during the next three forecast hours. The similarity

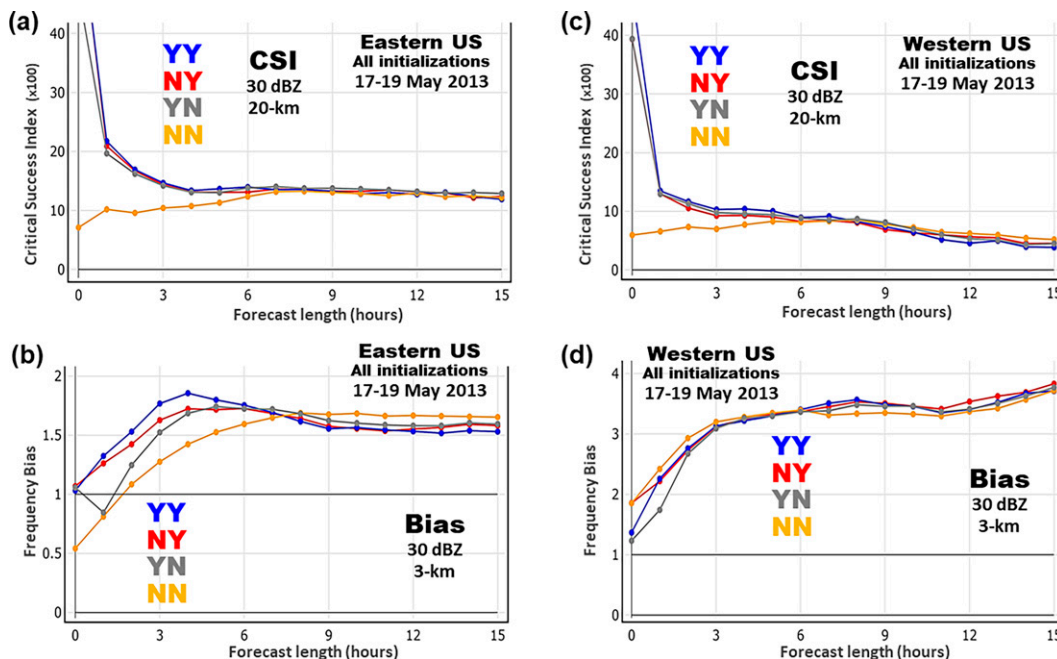


FIG. 6. Overall average categorical verification statistics for the 30-dBZ reflectivity threshold for the four experiments as a function of forecast length. (a),(c) The critical success index (CSI) up-scaled to a 20-km grid and (b),(d) the frequency bias on the native 3-km grid for (left) the eastern U.S. region and (right) the western U.S. region. See text for additional details.

of the CSI score over the entire forecast length for all three of these experiments (YY, YN, NY) is quite striking and indicates that the model convective response (for these convection-dominated cases) is quite similar for the different radar-LHI procedures. The CSI scores for these three experiments stand in contrast to the result for the NN experiment, which has no radar-LHI applied on either domain. For this experiment, the CSI is low at the initial time but increases with forecast length through the first 6–7 h, closely matching the other CSI scores thereafter. Comparison of the E region versus W region shows a greater benefit from the reflectivity assimilation for the E region during the first 3 h, with higher scores for all experiments for the E region through the entire 15-h forecast period. This is likely related to the larger scale for some of the convection over the E region and also a function of the very high bias in the W region, as seen in Fig. 6d.

Examination of the bias scores for the E region reveals modest differences among the three experiments with radar-LHI assimilation for the E region and similarly quite high bias values for the W region. The YY experiment has the highest bias through the first five forecast hours. We also see the application of the radar-LHI on only the 3-km HRRR domain (NY) initially yields a higher bias than application of the radar-LHI on only the 13-km RAP domain (YN), but these differences are gone by six hours into the model forecast. Overall, the average bias for the three radar-LHI experiments (YY, YN, NY) grows rapidly during the first few hours of the model forecast, reaching a maximum of about 1.8 at 4 h into the free forecast, then gradually decreasing to a value of about 1.6.

For the W region, bias values quickly grow to near 3.5 for all experiments, including the NN experiment with no reflectivity assimilation. While issues with the more limited radar coverage across the western United States are likely a factor in these high biases (especially for a high reflectivity threshold like 30 dBZ), these results support the notion that the model may have been too active with convection in the W region. For reference, the 3-km base rate (fraction of grid points with observed values above the threshold) values for reflectivity > 30 dBZ (averaged over all forecast lengths in Fig. 6) for the W and E regions are 0.007 and 0.018, respectively, indicating the significantly reduced MRMS coverage of 30-dBZ reflectivity over the W region. We have examined W region bias plots for lower reflectivity thresholds (25 and 20 dBZ), and they reveal differences from the W region 30-dBZ plot (Fig. 6d). For both lower thresholds, all three of the reflectivity assimilation experiments (YY, NY, YN) produce a modest lowering of the high reflectivity bias (compared to the NN experiment.) for the first six hours of the forecast. For the E region, the bias plots for the 25- and 20-dBZ reflectivity thresholds look similar to the E region 30-dBZ bias plot (Fig. 6b).

To further assess the diurnal aspects of the radar assimilation impact, we now show a comparison of CSI and bias scores as a function of forecast length for the four experiments for an average of five model initialization times during (i) the overnight ongoing convective period (0300, 0400, 0500, 0600, 0700 UTC) and (ii) the afternoon convective growth period (1800, 1900, 2000, 2100, 2200 UTC). While our sample size is limited (seven overnight cases and six afternoon cases), it enables a comparison of the radar data assimilation impacts for

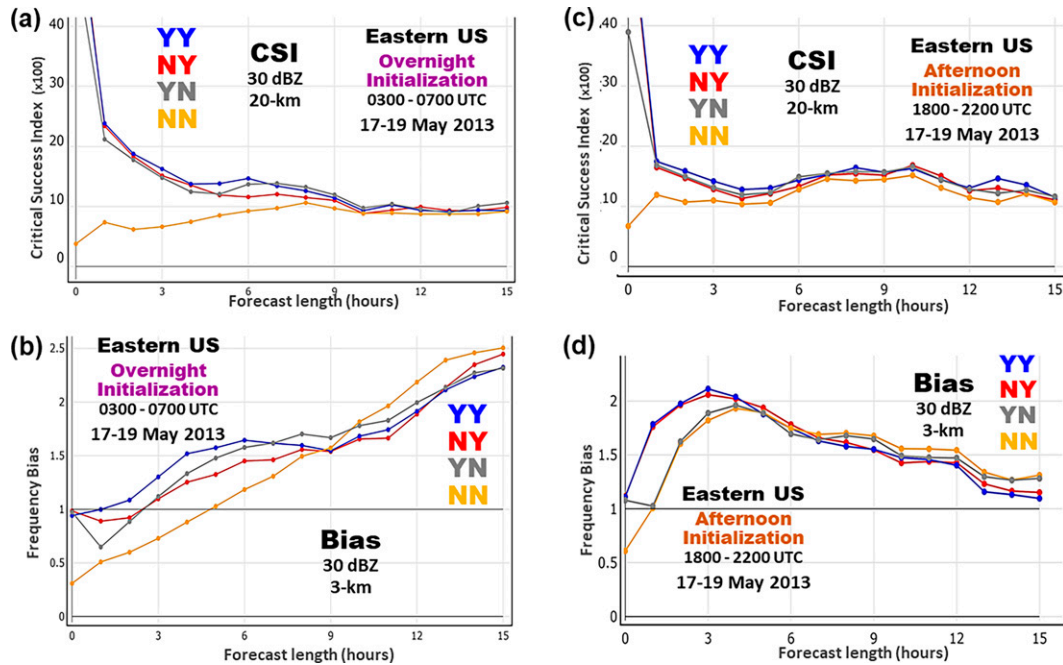


FIG. 7. Categorical verification statistics for the 30-dBZ reflectivity threshold for the four experiments as a function of forecast length for an average of (left) five overnight initialization times (0300, 0400, 0500, 0600, and 0700 UTC) and (right) five afternoon initialization times (1800, 1900, 2000, 2100, and 2200 UTC). (a),(c) The critical success index (CSI) up-scaled to a 20-km grid and (b),(d) frequency bias on the native 3-km grid, all for the eastern U.S. region. See text for additional details.

these two initialization time periods. Similar to Fig. 6, Fig. 7 shows a comparison of CSI and bias scores, but now for the five overnight initialization times versus the five afternoon initialization times for the E region. The CSI scores confirm the expectation that the radar assimilation technique is more successful for overnight initializations compared to afternoon initializations, with a greater skill score increase for the three assimilation experiments over the NN experiment for the first several forecast hours. This is consistent with the larger amount of ongoing observed convection likely occurring overnight and the likely greater difficulty during the overnight period of initiating new model convection (to catch up with missed convection), without the radar assimilation (due to the increased convective inhibition overnight). The bias evolutions are also distinctly different, with all experimental biases growing through the 15-h forecast period for the overnight initializations. Again, not surprisingly, the bias for the NN experiment is much lower than the other experiments (through about 8 h). We note that the enhanced bias increase beginning around 9 h may be associated with the morning time period of rapid decrease in observed convective coverage.

For the afternoon initialization times, the CSI improvement from the reflectivity assimilation is noticeably reduced in magnitude and duration. Interestingly, the degree of bias increase during the first few hours is amplified by the HRRR-based assimilation (experiments YY and NY). This is consistent with the smaller-scale latent heating during the HRRR pre-forecast hour immediately enabling convective development even without

any latent heating in the RAP. This is in contrast to the early overnight period, when the RAP heating in conjunction with the HRRR heating (experiment YY) yields a higher bias than the experiment with HRRR heating alone (NY).

Figure 8 shows a similar comparison for the W region and the diurnal impacts are even more pronounced. The CSI scores show modest forecast improvement from the radar assimilation for the first few hours for initializations during the overnight period, but only slight skill improvement for the initializations during the afternoon period. The bias plot for the afternoon initializations (Fig. 8b) shows similarly very high biases for all four experiments for the convectively active afternoon period and extending into the late evening (about the first eight forecast hours). While the limitations with the observed radar coverage in the west may have played a significant role in these high biases, these results suggest that the model likely produced an overly active diurnal cycle of convection over the W region that was independent of any radar assimilation. While further assessment of the various W region issues is beyond the scope of this paper, these results provide further information about the performance of the assimilation technique for different regions and show strong consistencies with the diurnal aspects seen in the E region verification. For the overnight initializations, the rapid increase in bias later in the forecast (beginning after forecast hour 11 in Fig. 8b, 1400–1800 UTC valid times) for all four experiments, may indicate the beginning of an overly active diurnal convective cycle in the model across the W region.

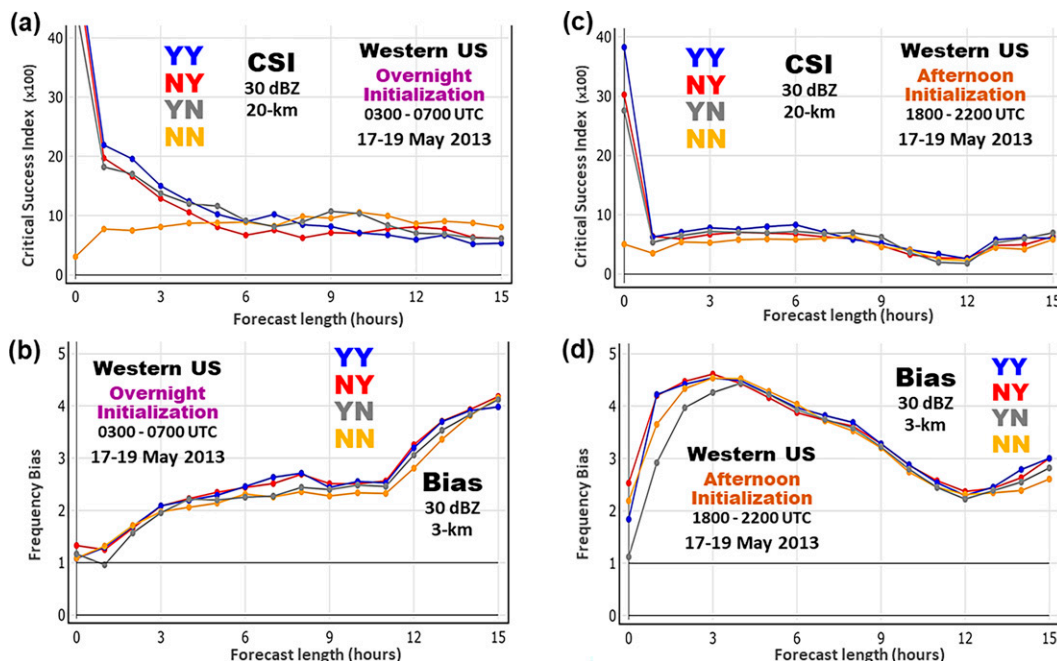


FIG. 8. As in Fig. 7, but all verification statistics are for the western U.S. region. See text for additional details.

d. Two case study assessments

To further illustrate some of the results seen above, we present short-range forecast images from two archetype cases: an overnight case with ongoing convective systems and an afternoon case with growing convection. Figure 9 shows the overnight case, with 15-min, 1-h, and 2-h forecast reflectivity fields from all four retrospective experiments for HRRR runs initialized at 0500 UTC 18 May 2013 [displayed over the northern plains region (Nebraska, South Dakota, North Dakota, Minnesota, Iowa), zoomed-in from the full HRRR integration domain]. Also shown are corresponding MRMS radar reflectivity analyses (over a matched region) for the three forecast times, indicating multiple ongoing convective systems over the region. The leftmost column shows the reflectivity field 15 min into the free-forecast period, providing clear evidence that the largest immediate (15 min) impact on the reflectivity field is from the inclusion of the forward-radar-LH in the HRRR 1-h pre-forecast initialization (YY and NY experiments). With no radar-LHI (in either the RAP or the HRRR, experiment NN), there is only weak scattered convection. This indicates that, for these experiments, the model was unable to reproduce most of the observed strong convection without the radar reflectivity assimilation in at least one of the model systems (RAP or HRRR). The reflectivity that does exist at 15 min in experiment NN is likely mostly from remnants of light gridscale precipitation in the RAP (interpolated to the HRRR domain in the preprocessing). Interestingly, application of radar-LHI within the RAP, but not the HRRR (experiment YN), results in very little strong (>40 dBZ) convective development during the 1-h pre-forecast (now without forward-radar-LH) and the first 15 min of the free-forecast, but strong convection does develop by 1 h. With no HRRR

forward-radar-LH, this convective development in the HRRR is due primarily to the induced low-level convergence and upper-level divergence resulting from the RAP radar-LH-DFI. Note that even for the two experiments with HRRR forward-radar-LH (YY and NY), noticeable differences exist in the 15-min reflectivity fields, with somewhat larger coverage of high reflectivity in the YY fields relative to the NY fields. By one hour, the YY and NY experiments have continued their respective developments, with the greatest small-scale intensity seen in the HRRR-only forward-radar-LH experiment (NY). We also see that, by 1-h, convective development is underway for the RAP-only radar-LH-DFI experiment (YN). In contrast, the experiment with no radar-LHI (in either RAP or HRRR, NN) still only shows minimal development. By 2-h, the YY and NY experiments look similar, but with slightly less coverage for the HRRR-only experiment (NY). The convective evolution in the RAP-only (YN) experiment is continuing to catch up, while the convective development in the NN experiment still significantly lags the other experiments.

We now contrast the above results with those from a simulation initialized much earlier in the diurnal convective cycle, when convection was rapidly developing and expanding in coverage. It is important to note that this time is near the time of maximum surface temperature for the day, so we expect there to be a relative minimum in convective inhibition (CI) and a greater ease of CI in the model with or without application of the radar-LHI. Similar to Fig. 9, Fig. 10 shows the 15-min, 1-h, and 2-h HRRR forecast reflectivity fields from all four experiments, but now for a 2200 UTC 17 May 2013 model initialization time, focusing on a growing convective line that developed as a small cluster of storms during the 2000–2100 UTC

Initial conditions – 0500 UTC 18 May 2013

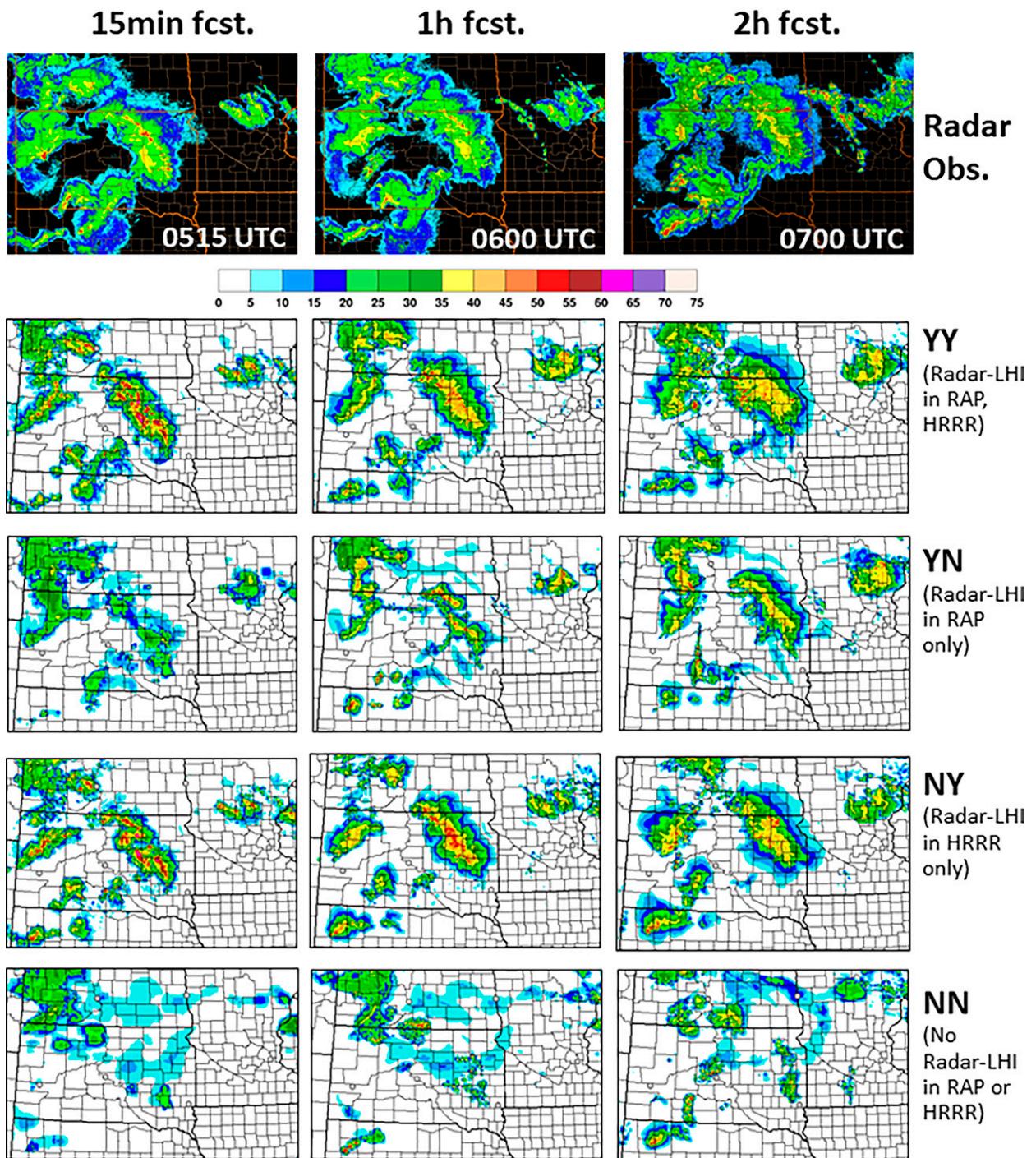


FIG. 9. HRRR 15-min, 1-h, and 2-h forecast composite reflectivity fields (from a portion of the HRRR domain) for all four radar-LHI experiments for the overnight ongoing convection case (model initialization at 0500 UTC 18 May 2013). Also shown are the corresponding MRMS observed composite reflectivity fields. The reflectivity color bar (dBZ) is shown near the top of the figure. See text for additional details.

Initial conditions – 2200 UTC 17 May 2013

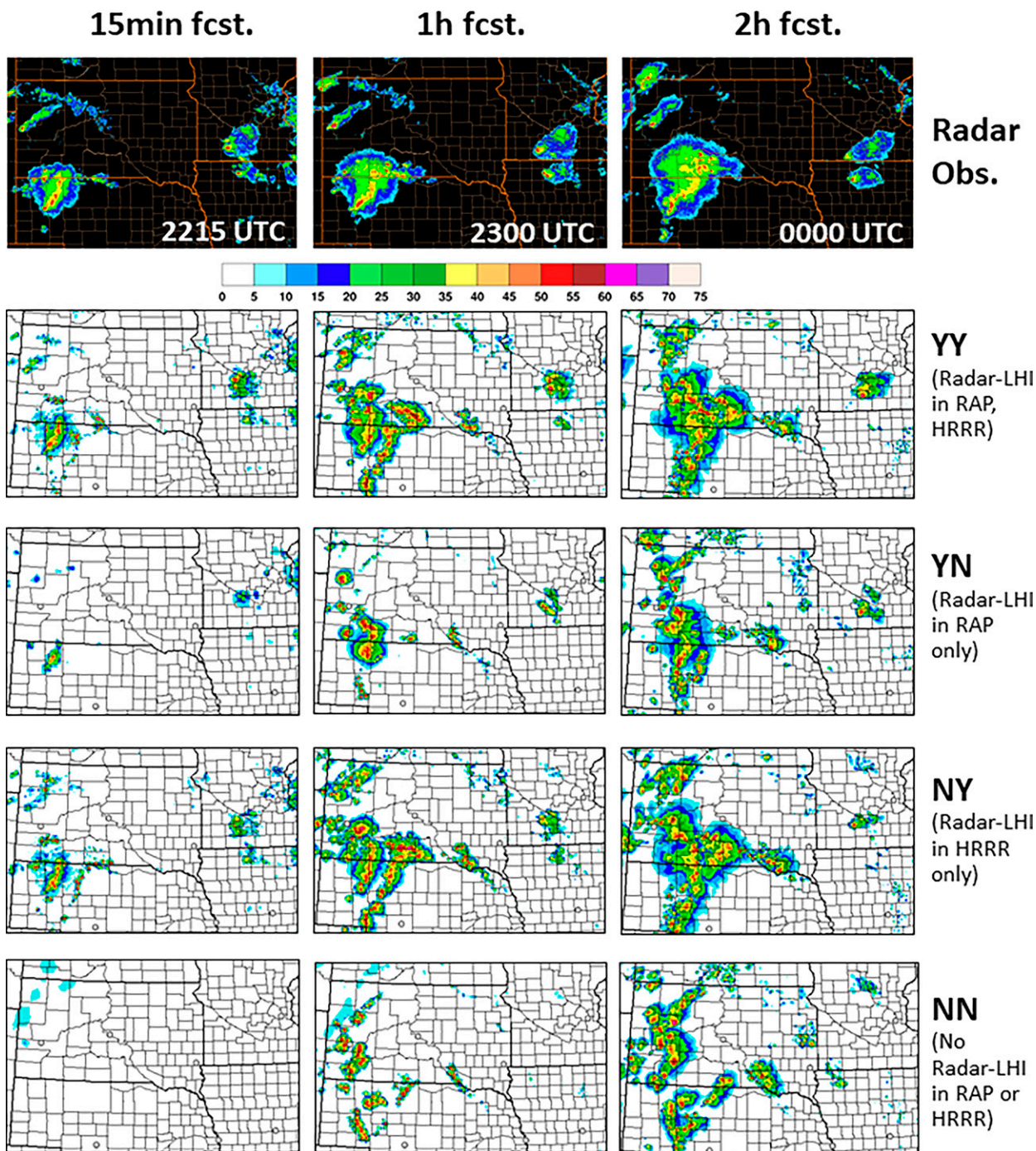


FIG. 10. As in Fig. 9, but for the afternoon growing convection case (model initialization at 2200 UTC 17 May 2013).

time period, with the pre-forecast period occurring just after that from 2100 to 2200 UTC.

In addition to illustrating the performance of the different experiments for a case with model initialization during the afternoon storm growth time period, this case provides an

interesting example of a potential issue that can occur when the forward-radar-LH is applied during the 1-h pre-forecast of the HRRR. The 15-min forecast fields in the left column show somewhat expected results, with representation of the observed short squall-line segment over northwest Nebraska

in all three of the radar-LHI runs and no clear depiction of it in the NN run. Further examination of the two runs with the HRRR forward-radar-LH (YY and NY) reveals another weak line segment in advance of the main one. This is especially evident in the NY experiment. Detailed assessment of fields from the YY and NY runs (not shown) indicates that, for this case, the forward-radar-LH operating over the hour-long pre-forecast period in the 3-km HRRR generated a forward propagating low-level outflow boundary that, in conjunction with a weak preexisting environmental boundary, served as a focusing mechanism for the generation of the spurious leading line. The 1-h forecasts shown in the middle column show the continued development of this leading line in the two HRRR forward-radar-LH experiments (YY and NY), relative to the experiment with just radar-LH-DFI in the RAP (YN). Also, some weak development along the preexisting boundary is now evident in the run with no radar-LHI (NN). It is interesting to note that while the 1-h forecast from the run with radar-LHI only in the RAP (YN) does not show a realistic line-like structure, this experiment avoids the spurious leading line development found in the YY and NY experiments. Limitations of the study preclude further detailed assessment of this run, but consistent with the example in Fig. 6, application of the radar-LHI on a larger scale within the RAP (compared to the HRRR) creates a larger-scale low-level convergence/upper-level divergence field focused around the radar-observed storms that may be helping to inhibit nearby storm development. By 2 h into the forecast (right column), the four experiments are more similar, though the convective evolution in NN still lags that of the other experiments. Interestingly, at 2 h a leading line has developed in the RAP-only radar-LH-DFI experiment (YN), while in the YY and NY experiments the two lines from the 1-h forecasts appear to have merged somewhat.

4. Summary and conclusions

An innovative assimilation technique using radar reflectivity data to initialize NOAA operational weather prediction models is described in this paper. This technique, which uses latent heating specified from radar reflectivity (and can also accommodate lightning data and other indicators of convection or precipitation), was first implemented in 2009 at NCEP and continues to be used in 2022 in the NCEP-operational RAP and HRRR models. This study provides documentation of the performance of two formulations (related procedures) of a radar reflectivity-based latent heating initialization (radar-LHI) technique. The first procedure (radar-LH-DFI), originally developed for the RUC, is applied in the 13-km RAP and involves specification of a radar reflectivity-based temperature tendency in the forward model portion of the diabatic digital filter initialization (DFI). This temperature tendency is derived from the latent heating estimate based on reflectivity and an assumed convective time scale, and is used in the DFI in place of the temperature tendency calculated from the explicit microphysics and the cumulus parameterization. For the 3-km HRRR procedure (forward-radar-LH), no DFI is used, and the temperature tendency is specified during an hour-

long model pre-forecast forward integration period. In this paper we document the reflectivity forecast improvement in the HRRR from application of the radar-LHI in the RAP, HRRR, and in both the RAP and HRRR. We also provide an illustration of the time evolution of the forecast reflectivity for all the experiments for two archetype times: afternoon just after CI and overnight with ongoing mature convection. Differences in the behavior of the various radar-LHI applications for these different times of day are highlighted.

This radar-LHI technique has been a backbone of the NOAA rapidly updated numerical weather prediction capability since 2009, and it is important to document the technique and the behavior of its different formulations. For the convective period studied here, it produces a significant improvement in short-range reflectivity forecasts (through about 6 h). This improvement was seen both in average CSI statistics and individual case study images. While use of the radar-LHI technique for either the RAP or the HRRR results in somewhat excessive convection for the first few hours of the model forecast (as indicated by the elevated bias score), the CSI scores are clearly improved during this period and the impacts of the radar-LHI diminish gradually, leading to leveling of the CSI scores to near the no radar-LHI average values by about the 7-h forecast mark. Reductions in the strength of the latent heating in the RAP for more recent RAP/HRRR versions (see Table 2) have yielded a reduction in the elevated bias scores for the very short-range forecasts (see Fig. 2 in J22).

In addition to documenting the improvement in reflectivity forecast skill for different combinations of the radar-LHI technique for eastern versus western U.S. regions, we have illustrated differences in the forecast impact between two archetype periods of the diurnal cycle (afternoon and overnight), for the eastern and western regions. These diurnal and regional performance differences are consistent with the diurnal and regional differences in observed convection and regional radar coverage differences. Documentation of these performance aspects is useful for evaluating the utility and limitations of the technique and as a benchmark for exploration of improved reflectivity assimilation methods.

For the RAPv5/HRRRv4, which was operationally implemented at NCEP on 2 December 2020, we have retained the radar-LHI for both the RAP and the HRRR, but are supplementing it with an ensemble Kalman filter (EnKF)-based radar reflectivity algorithm for the HRRR, which is applied within the HRRRDAS (D22). A DA flowchart comparison between HRRRv3 and HRRRv4 is provided in D22 (their Fig. 3). Versions of the radar-LHI and EnKF-based reflectivity assimilation techniques will be used in the future NOAA Rapid Refresh Forecast System (RRFS) which is slated to replace the NOAA operational RAPv5/HRRRv4, and this will be described in future papers. Slightly modified forms of this radar-LHI technique have also been used experimentally to assimilate satellite-based cloud-top cooling rate data (Mecikalski et al. 2008) and GOES-R Geostationary Lightning Mapper data (Rudlosky et al. 2019).

Acknowledgments. This project is primarily supported by NOAA Research and the Federal Aviation Administration

(FAA). This research is in response, in part, to requirements from and funding by the FAA. The views expressed are those of the authors and do not necessarily represent the official policy or position of the FAA. We thank Jeff Hamilton and Molly Smith at NOAA/GSL for their excellent work with the MATS verification database. We also thank Amanda Back of NOAA/GSL for a very helpful review of the manuscript and the NOAA/HPC and NOAA/GSL/ITS staff for providing computing resources for this work.

Data availability statement. The observations and other data used in this research are housed within the NOAA Global Systems Laboratory (GSL) data archive.

REFERENCES

- Aksoy, A., D. C. Dowell, and C. Snyder, 2009: A multicaser comparative assessment of the ensemble Kalman filter for assimilation of radar observations. Part I: Storm-scale analyses. *Mon. Wea. Rev.*, **137**, 1805–1824, <https://doi.org/10.1175/2008MWR2691.1>.
- , —, and —, 2010: A multicaser comparative assessment of the ensemble Kalman filter for assimilation of radar observations. Part II: Short-range ensemble forecasts. *Mon. Wea. Rev.*, **138**, 1273–1292, <https://doi.org/10.1175/2009MWR3086.1>.
- Benjamin, S. G., and Coauthors, 2004: An hourly assimilation/forecast cycle: The RUC. *Mon. Wea. Rev.*, **132**, 495–518, [https://doi.org/10.1175/1520-0493\(2004\)132<0495:AHACTR>2.0.CO;2](https://doi.org/10.1175/1520-0493(2004)132<0495:AHACTR>2.0.CO;2).
- , and Coauthors, 2016: A North American hourly assimilation and model forecast cycle: The Rapid Refresh. *Mon. Wea. Rev.*, **144**, 1669–1694, <https://doi.org/10.1175/MWR-D-15-0242.1>.
- , and Coauthors, 2021: Stratiform cloud-hydrometeor assimilation for HRRR and RAP model short-range weather prediction. *Mon. Wea. Rev.*, **149**, 2673–2694, <https://doi.org/10.1175/MWR-D-20-0319.1>.
- Carbone, R. E., and J. D. Tuttle, 2008: Rainfall occurrence in the U.S. warm season: The diurnal cycle. *J. Climate*, **21**, 4132–4146, <https://doi.org/10.1175/2008JCLI2275.1>.
- Caya, A., J. Sun, and C. Snyder, 2005: A comparison between the 4DVAR and the ensemble Kalman filter techniques for radar data assimilation. *Mon. Wea. Rev.*, **133**, 3081–3094, <https://doi.org/10.1175/MWR3021.1>.
- Chen, H., J. Gao, Y. Wang, Y. Chen, T. Sun, J. Carlin, and Y. Zheng, 2021: Radar reflectivity data assimilation method based on background-dependent hydrometeor retrieval: The comparison with direct assimilation in real cases. *Quart. J. Roy. Meteor. Soc.*, **147**, 2409–2428, <https://doi.org/10.1002/qj.4031>.
- Danard, M. B., 1964: On the influence of released latent heat on cyclone development. *J. Appl. Meteor.*, **3**, 27–37, [https://doi.org/10.1175/1520-0450\(1964\)003<0027:OTIORL>2.0.CO;2](https://doi.org/10.1175/1520-0450(1964)003<0027:OTIORL>2.0.CO;2).
- Doswell, C. A., R. Davies-Jones, and D. L. Keller, 1990: On summary measures of skill in rare event forecasting based on contingency tables. *Wea. Forecasting*, **5**, 576–585, [https://doi.org/10.1175/1520-0434\(1990\)005<0576:OSMOSI>2.0.CO;2](https://doi.org/10.1175/1520-0434(1990)005<0576:OSMOSI>2.0.CO;2).
- Dowell, D. C., and Coauthors, 2022: The High-Resolution Rapid Refresh (HRRR): An hourly updating convection-permitting forecast model. Part I: Motivation and system description. *Wea. Forecasting*, in press, <https://doi.org/10.1175/WAF-D-21-0151.1>.
- Duda, J. D., X. Wang, Y. Wang, and J. R. Carley, 2019: Comparing the assimilation of radar reflectivity using the direct GSI-based ensemble-variational (EnVar) and indirect cloud analysis methods in convection-allowing forecasts over the continental United States. *Mon. Wea. Rev.*, **147**, 1655–1678, <https://doi.org/10.1175/MWR-D-18-0171.1>.
- Ebert, E. E., 2009: Neighborhood verification: A strategy for rewarding close forecasts. *Wea. Forecasting*, **24**, 1498–1510, <https://doi.org/10.1175/2009WAF2222251.1>.
- Fabry, F., V. Meunier, B. Puigdomènech Treserras, A. Cournoyer, and B. Nelson, 2017: On the climatological use of radar data composites: Possibilities and challenges. *Bull. Amer. Meteor. Soc.*, **98**, 2135–2148, <https://doi.org/10.1175/BAMS-D-15-00256.1>.
- Fiorino, M., and T. T. Warner, 1981: Incorporating surface winds and rainfall rates into the initialization of a mesoscale hurricane model. *Mon. Wea. Rev.*, **109**, 1914–1929, [https://doi.org/10.1175/1520-0493\(1981\)109<1914:ISWARR>2.0.CO;2](https://doi.org/10.1175/1520-0493(1981)109<1914:ISWARR>2.0.CO;2).
- Grell, G. A., and S. R. Freitas, 2014: A scale and aerosol aware stochastic convective parameterization for weather and air quality modeling. *Atmos. Chem. Phys.*, **14**, 5233–5250, <https://doi.org/10.5194/acp-14-5233-2014>.
- Gustafsson, N., and Coauthors, 2018: Survey of data assimilation methods for convective-scale numerical weather prediction at operational centres. *Quart. J. Roy. Meteor. Soc.*, **144**, 1218–1256, <https://doi.org/10.1002/qj.3179>.
- Hawkness-Smith, L. D., and D. Simonin, 2021: Radar reflectivity assimilation using hourly cycling 4D-Var in the Met Office Unified Model. *Quart. J. Roy. Meteor. Soc.*, **147**, 1516–1538, <https://doi.org/10.1002/qj.3977>.
- Hu, M., S. G. Benjamin, T. T. Ladwig, D. C. Dowell, S. S. Weygandt, C. R. Alexander, and J. S. Whitaker, 2017: GSI three-dimensional ensemble-variational hybrid data assimilation using a global ensemble for the regional Rapid Refresh model. *Mon. Wea. Rev.*, **145**, 4205–4225, <https://doi.org/10.1175/MWR-D-16-0418.1>.
- Huang, X.-Y., and P. Lynch, 1993: Diabatic digital filter initialization: Application to the HIRLAM model. *Mon. Wea. Rev.*, **121**, 589–603, [https://doi.org/10.1175/1520-0493\(1993\)121<0589:DDFIAT>2.0.CO;2](https://doi.org/10.1175/1520-0493(1993)121<0589:DDFIAT>2.0.CO;2).
- Huang, Y., and Coauthors, 2018: Forecasting severe convective storms with WRF-based RTFDDA radar data assimilation in Guangdong, China. *Atmos. Res.*, **209**, 131–143, <https://doi.org/10.1016/j.atmosres.2018.03.010>.
- Huo, Z., Y. Liu, M. Wei, Y. Shi, C. Fang, Z. Shu, and Y. Li, 2021: Hydrometeor and latent heat nudging for radar reflectivity assimilation: Response to the model states and uncertainties. *Remote Sens.*, **13**, 3821, <https://doi.org/10.3390/rs13193821>.
- Jacques, D., D. Michelson, J.-F. Caron, and L. Fillion, 2018: Latent heat nudging in the Canadian regional deterministic prediction system. *Mon. Wea. Rev.*, **146**, 3995–4014, <https://doi.org/10.1175/MWR-D-18-0118.1>.
- James, E. P., and Coauthors, 2022: The High-Resolution Rapid Refresh (HRRR): An hourly updating convection-allowing forecast model. Part II: Forecast performance. *Wea. Forecasting*, in press, <https://doi.org/10.1175/WAF-D-21-0130.1>.
- Jones, C. D., and B. Macpherson, 1997: A latent heat nudging scheme for the assimilation of precipitation data into an operational mesoscale model. *Meteor. Appl.*, **4**, 269–277, <https://doi.org/10.1017/S1350482797000522>.
- Kelleher, K. E., and Coauthors, 2007: Project CRAFT: A real-time delivery system for NEXRAD Level-II data via the

- Internet. *Bull. Amer. Meteor. Soc.*, **88**, 1045–1057, <https://doi.org/10.1175/BAMS-88-7-1045>.
- Klazura, G. E., and D. A. Imy, 1993: A description of the initial set of analysis products available from the NEXRAD WSR-88D system. *Bull. Amer. Meteor. Soc.*, **74**, 1293–1311, [https://doi.org/10.1175/1520-0477\(1993\)074<1293:ADOTIS>2.0.CO;2](https://doi.org/10.1175/1520-0477(1993)074<1293:ADOTIS>2.0.CO;2).
- Leuenberger, D., and A. Rossa, 2007: Revisiting the latent heat nudging scheme for the rainfall assimilation of a simulated convective storm. *Meteor. Atmos. Phys.*, **98**, 195–215, <https://doi.org/10.1007/s00703-007-0260-9>.
- Lynch, P., and X.-Y. Huang, 1992: Initialization of the HIRLAM model using a digital filter. *Mon. Wea. Rev.*, **120**, 1019–1034, [https://doi.org/10.1175/1520-0493\(1992\)120<1019:IOTHMU>2.0.CO;2](https://doi.org/10.1175/1520-0493(1992)120<1019:IOTHMU>2.0.CO;2).
- , and —, 1994: Diabatic initialization using recursive filters. *Tellus*, **46A**, 583–597, <https://doi.org/10.3402/tellusa.v46i5.15646>.
- Marshall, J. S., and W. McK. Palmer, 1948: The distribution of raindrops with size. *J. Meteor.*, **5**, 165–166, [https://doi.org/10.1175/1520-0469\(1948\)005<0165:TDORWS>2.0.CO;2](https://doi.org/10.1175/1520-0469(1948)005<0165:TDORWS>2.0.CO;2).
- Martet, M., P. Brousseau, E. Wattrelot, F. Guillaume, and J.-F. Mahfouf, 2022: Operational assimilation of radar data from the European EUMETNET Programme OPERA in the Météo-France convective-scale model AROME. *Data Assimilation for Atmospheric, Oceanic and Hydrologic Applications*. Vol. IV, S. K. Park and L. Xu, Eds., Springer, 629–644, https://doi.org/10.1007/978-3-030-77722-7_24.
- Mecikalski, J. R., K. M. Bedka, S. J. Paech, and L. A. Litten, 2008: A statistical evaluation of GOES cloud-top properties for predicting convective initiation. *Mon. Wea. Rev.*, **136**, 4899–4914, <https://doi.org/10.1175/2008MWR2352.1>.
- Peckham, S. E., T. G. Smirnova, S. G. Benjamin, J. M. Brown, and J. S. Kenyon, 2016: Implementation of a digital filter initialization in the WRF Model and application in the Rapid Refresh. *Mon. Wea. Rev.*, **144**, 99–106, <https://doi.org/10.1175/MWR-D-15-0219.1>.
- Rudlosky, S. D., S. J. Goodman, K. S. Virts, and E. C. Bruning, 2019: Initial geostationary lightning mapper observations. *Geophys. Res. Lett.*, **46**, 1097–1104, <https://doi.org/10.1029/2018GL081052>.
- Sauer, M., M. Steiner, R. D. Sharman, J. O. Pinto, and W. Deierling, 2019: Tradeoffs for routing flights in view of multiple weather hazards. *J. Air Transp.*, **27**, 70–80, <https://doi.org/10.2514/1.D0124>.
- Stephan, K., S. Klink, and C. Schraff, 2008: Assimilation of radar-derived rain rates into the convective-scale model COSMO-DE at DWD. *Quart. J. Roy. Meteor. Soc.*, **134**, 1315–1326, <https://doi.org/10.1002/qj.269>.
- Sun, J., and N.A. Crook, 1997: Dynamical and microphysical retrieval from Doppler radar observations using a cloud model and its adjoint. Part I: Model development and simulated data experiments. *J. Atmos. Sci.*, **54**, 1642–1661, [https://doi.org/10.1175/1520-0469\(1997\)054<1642:DAMRFD>2.0.CO;2](https://doi.org/10.1175/1520-0469(1997)054<1642:DAMRFD>2.0.CO;2).
- , and —, 1998: Dynamical and microphysical retrieval from Doppler radar observations using a cloud model and its adjoint. Part II: Retrieval experiments of an observed Florida convective storm. *J. Atmos. Sci.*, **55**, 835–852, [https://doi.org/10.1175/1520-0469\(1998\)055<0835:DAMRFD>2.0.CO;2](https://doi.org/10.1175/1520-0469(1998)055<0835:DAMRFD>2.0.CO;2).
- Wang, H., J. Sun, X. Zhang, X.-Y. Huang, and T. Auligne, 2013: Radar data assimilation with WRF 4D-Var. Part I: System development and preliminary testing. *Mon. Wea. Rev.*, **141**, 2224–2244, <https://doi.org/10.1175/MWR-D-12-00168.1>.
- Wang, W., and T. T. Warner, 1988: Use of four-dimensional data assimilation by Newtonian relaxation and latent-heat forcing to improve a mesoscale-model precipitation forecast: A case study. *Mon. Wea. Rev.*, **116**, 2593–2612, [https://doi.org/10.1175/1520-0493\(1988\)116<2593:UOFDDA>2.0.CO;2](https://doi.org/10.1175/1520-0493(1988)116<2593:UOFDDA>2.0.CO;2).
- Wang, Y., P. S. Skinner, K. Knopfmeier, T. Jones, G. Creager, P. L. Heiselman, and L. J. Whicker, 2019: Test of a weather-adaptive dual-resolution hybrid Warn-on-Forecast analysis and forecast system for several severe weather events. *Wea. Forecasting*, **34**, 1807–1827, <https://doi.org/10.1175/WAF-D-19-0071.1>.
- Wattrelot, E., O. Caumont, and J.-F. Mahfouf, 2014: Operational implementation of the 1D+3D-Var assimilation method of radar reflectivity data in the AROME model. *Mon. Wea. Rev.*, **142**, 1852–1873, <https://doi.org/10.1175/MWR-D-13-00230.1>.
- Weygandt, S. S., A. F. Loughe, S. G. Benjamin, and J. L. Mahoney, 2004: Scale sensitivities in model precipitation skill scores during IHOP. *22nd Conf. on Severe Local Storms*, Hyannis, MA, Amer. Meteor. Soc., 16A.8, <https://ams.confex.com/ams/11aram22sls/webprogram/Paper81986.html>.
- , M. Hu, S. G. Benjamin, T. G. Smirnova, K. J. Brundage, and J. M. Brown, 2008: Assimilation of lightning data using a digital filter within the rapid update cycle. *Proc. Second Int. Lightning Meteorology Conf.*, Tucson, AZ, Vaisala, <https://www.vaisala.com/sites/default/files/documents/Assimilation%20of%20Lightning%20Data%20Using%20a%20Diabatic%20Digital%20Filter%20Within%20the%20Rapid%20Update%20Cycle.PDF>.
- Wheatley, D. M., K. H. Knopfmeier, T. A. Jones, and G. J. Creager, 2015: Storm-scale DA and ensemble forecasting with the NSSL experimental Warn-on-Forecast system. Part I: Radar data experiments. *Wea. Forecasting*, **30**, 1795–1817, <https://doi.org/10.1175/WAF-D-15-0043.1>.
- Zhang, J., and Coauthors, 2011: National Mosaic and Multi-Sensor QPE (NMQ) system: Description, results, and future plans. *Bull. Amer. Meteor. Soc.*, **92**, 1321–1338, <https://doi.org/10.1175/2011BAMS-D-11-00047.1>.
- , and Coauthors, 2016: Multi-Radar Multi-Sensor (MRMS) quantitative precipitation estimation: Initial operating capabilities. *Bull. Amer. Meteor. Soc.*, **97**, 621–638, <https://doi.org/10.1175/BAMS-D-14-00174.1>.